J. Fluid Mech. (1995), vol. 298, pp. 113–137

Modelling and analysis of meniscus roll coating

By P. H. GASKELL[1], M. D. SAVAGE[2], J. L. SUMMERS[1] AND H. M. THOMPSON[2]

[1]Department of Mechanical Engineering, University of Leeds, LEEDS, LS2 9JT, UK
[2]Department of Applied Mathematical Studies, University of Leeds, LEEDS, LS2 9JT, UK

(Received 23 August 1994 and in revised form 15 December 1994)

Three mathematical models are developed for meniscus roll coating in which there is steady flow of a Newtonian fluid in the narrow gap, or nip, between two contra-rotating rolls in the absence of body forces.

The zero flux model predicts a constant pressure gradient within the central core and two eddies, each with an inner structure, in qualitative agreement with observation. The small flux model takes account of a small inlet flux and employs the lubrication approximation to represent fluid velocity as a combination of Couette and Poiseuille flows. Results show that the meniscus coating regime is characterized by small flow rates ($\lambda \ll 1$) and a sub-ambient pressure field generated by capillary action at the upstream meniscus. Such flows are found to exist for small modified capillary number, $Ca(R/H_0)^{1/2} \lesssim 0.15$, where Ca and R/H_0 represent capillary number and the radius to semi-gap ratio, respectively.

A third model incorporates the full effects of curved menisci and nonlinear free surface boundary conditions. The presence of a dynamic contact line, adjacent to the web on the upper roll, requires the imposition of an apparent contact angle and slip length. Numerical solutions for the velocity and pressure fields over the entire domain are obtained using the finite element method. Results are in accord with experimental observations that the flow domain consists of two large eddies and fluid transfer jets or 'snakes'. Furthermore, the numerical results show that the sub-structure of each large eddy consists of a separatrix with one saddle point, two sub-eddies with centres, and an outer recirculation.

Finally finite element solutions in tandem with lubrication analysis establish the existence of three critical flow rates corresponding to a transformation of the pressure field, the emergence of a 'secondary snake' (another fluid transfer jet) and the disappearance of a primary snake.

1. Introduction

The fluid mechanics of roll coating, with rigid rolls operating in either forward or reverse mode, has been extensively researched. Figure 1 illustrates forward mode coating in which the rolls of radius R_1 and R_2 move in the same direction through the nip with peripheral speeds U_1 and U_2, respectively. A fluid film of thickness H_i is picked up from a coating pan by the action of viscous lifting and enters the nip where the minimum gap thickness is $2H_0$. There are two coating regimes of practical

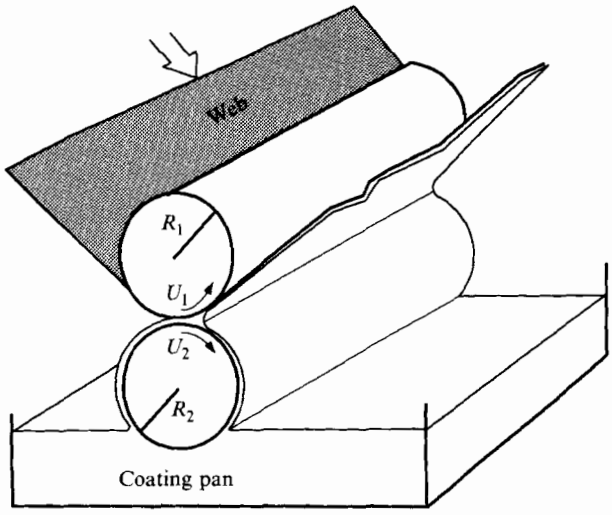

FIGURE 1. Schematic of a two-roll coater operating in forward mode.

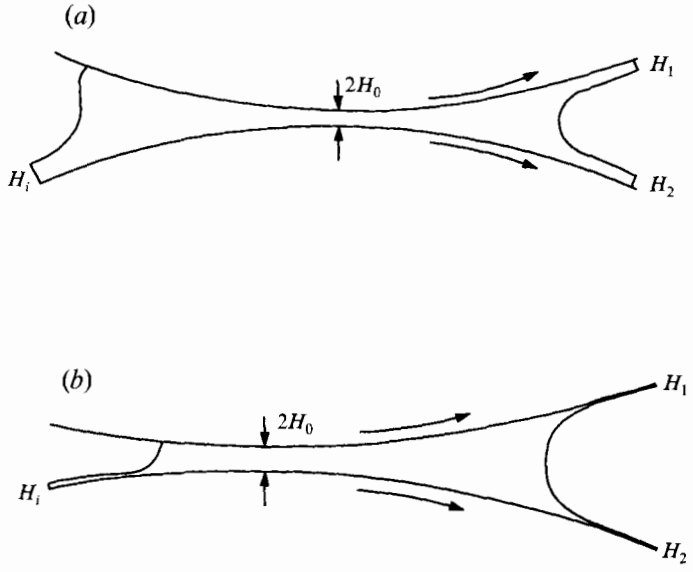

FIGURE 2. Magnified view of the nip region of a two-roll coater showing (*a*) a flooded inlet, (*b*) a starved inlet typical for meniscus roll coating.

importance, each identified according to the inlet feed condition, Malone (1992). They are the classical (inlet-flooded) regime and the meniscus (inlet-starved) regime as illustrated in figures 2(*a*) and 2(*b*), respectively. The former is the most familiar, for which there has been a wide range of experimental, analytical and computational investigations. These include the measurement and prediction of flux and film thickness (Pitts & Greiller 1961; Hintermaier & White 1965; Benkreira, Edwards & Wilkinson 1981; Savage 1982, 1984) together with pressure and velocity field distributions (Greener & Middleman 1975, 1979; Schneider 1962; Coyle, Macosko & Scriven 1986, 1987, 1990*a*,*b*; Coyle 1992).

Though used in industry for many years (Gaskell & Savage 1995), meniscus roll

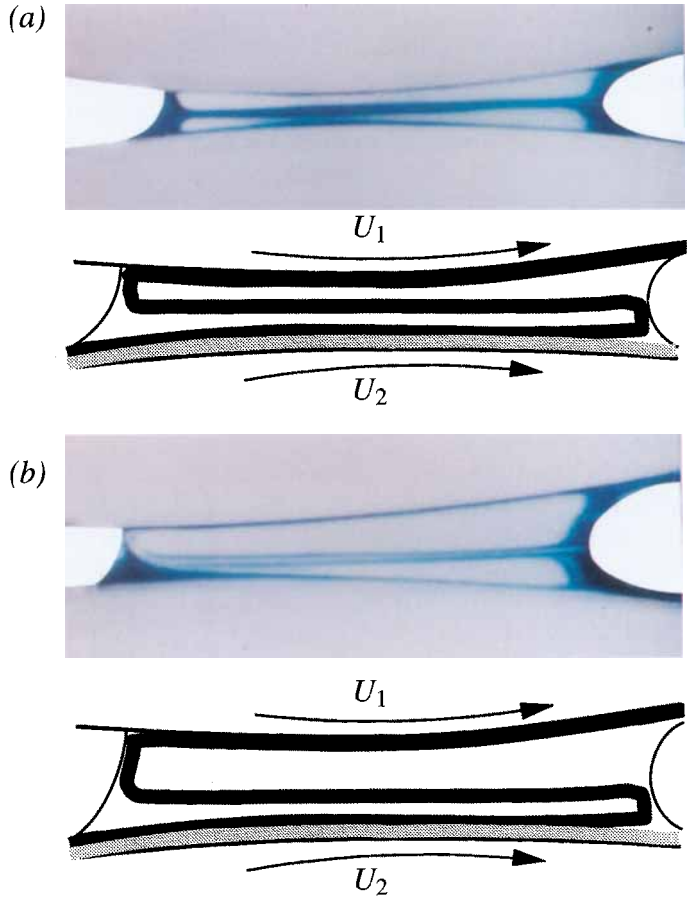

FIGURE 3. Actual and schematic dye traces, showing the flow in the bead of a meniscus roll coater with $R/H_0 = 125$ and rolls moving left to right: (*a*) $S = 1$; (*b*) $S = 2$.

coating appears to have escaped the attention of the coating community at large. Lack of references in the literature is perhaps due to an assumption by practitioners and theoreticians alike that this coating regime was essentially no different to the inlet-flooded regime. With the first experimental investigation of meniscus roll coating Malone (1992) demonstrated clearly the fallacy of such an assumption. His work showed the flow domain to be that of a 'small bead' located in the nip and extending along the length of the rolls. Axial velocity is negligible and the flow is thus two-dimensional as shown in figure 3(*a*,*b*) for speed ratio $S = 1$ and $S = 2$, where $S = U_1/U_2$. In each case the flow is observed to consist of two large eddies and a primary fluid transfer jet, or 'snake', transferring fluid to the web on the upper roll.

Three mathematical models for inlet-starved roll coating are presented, two of which are solved analytically and the third numerically. In the 'zero flux' model, the coating bead is assumed to be rectangular in cross-section with the menisci modelled as planes on which shear stress is zero and flux through the bead is neglected. Mathematically, the model reduces to the solution of a boundary value problem for the streamfunction which is similar to the driven cavity problems studied by Pan &

Acrivos (1967) and Canedo & Denson (1989). A solution for the streamfunction is obtained analytically in the form of a truncated series of eigenfunctions.

A 'small flux' model is formulated to take into account a small non-zero flow rate with $H_i/H_0 \ll 1$. Following a suggestion by S. M. Richardson (1988, personal communication) the flow in the centre of the bead is modelled as a combination of Couette and Poiseuille flow, thus giving rise to Reynolds' equation for the pressure distribution within the bead.

Though these analytical models do provide valuable insight into the flow structure and relationships between flow parameters, nevertheless they cannot reveal a complete picture. A more refined model is needed to take account of a dynamic contact line and nonlinear boundary conditions on two free surfaces whose shape and location are not known *a priori*. A dynamic contact line is where a free surface intersects a moving web at a well defined angle (Burley & Kennedy 1976) and where the precise boundary conditions are still a matter of some debate (Dussan V. 1979; De Gennes 1985).

Nonlinear boundary value problems of this sort require a numerical solution and because of its topological flexibility use was made of the finite element method (Zienkiewicz 1982), together with an appropriate free-surface parametric representation – see, for example, Kistler & Scriven (1983). Such methods were first applied to inlet-flooded, symmetric ($U_1 = U_2$), forward roll coating by Coyle *et al.* (1986) and subsequently extended to accommodate both unequal roll speeds and non-Newtonian rheology (Coyle *et al.* 1987). More recent investigations included an analysis of flow stability (Coyle *et al.* 1990*a*) and reverse roll coating (Coyle *et al.* 1990*b*). In all this work, except for reverse roll coating, only the downstream end was solved thus simplifying the problem quite considerably. The assumption of a flooded inlet allowed the region of interest to be terminated by appropriate boundary conditions at the point of minimum roll separation; it also removed the difficulty associated with the presence of a dynamic contact line, reducing the problem to the case of just one free surface.

The numerical solutions reported here not only complement the work of these authors, they represent also perhaps some of the most revealing and detailed computational results for fixed-gap forward roll coating available currently.

2. Zero flux model and eigenfunction solution

The two characteristic features of a meniscus roll coater are a substantially reduced inlet film and a fluid bead located in the nip between the moving rolls.

Central to the zero flux model is the assumption of negligible flux since the inlet flux is typically less than one tenth of that for an inlet-flooded roll coater. Additional assumptions include:

(i) a Newtonian fluid of constant density ρ and viscosity μ;

(ii) steady flow with negligible axial velocity, fluid inertia and body forces;

(iii) a closed and rectangular fluid domain of height $2H_0$ and width $2L_0$. The curvature of both the rolls and the free surfaces is assumed to be small so that the former can be modelled by horizontally moving flat plates and the latter by planes of zero shear stress. Consequently the normal stress condition at the free surface is redundant for the solution of this boundary value problem. It would only be used to provide a first-order correction to the free surface shape.

In the usual notation, with velocity components $\boldsymbol{U} = (U, W)$ and pressure $P(X, Z)$,

the flow is described by Stokes' equations:

$$\left.\begin{aligned} 0 &= \frac{\partial P}{\partial X} - \mu\nabla^2 U, \\ 0 &= \frac{\partial P}{\partial Z} - \mu\nabla^2 W, \end{aligned}\right\} \tag{2.1}$$

$$0 = \frac{\partial U}{\partial X} + \frac{\partial W}{\partial Z}\,, \tag{2.2}$$

for which the solution is expressed in terms of a streamfunction $\Psi(X,Z)$:

$$U = \frac{\partial \Psi}{\partial Z}\,,\quad W = -\frac{\partial \Psi}{\partial X}\,, \tag{2.3}$$

where Ψ is the solution of the biharmonic equation:

$$\nabla^4 \Psi = 0\,. \tag{2.4}$$

Suitable non-dimensional variables are

$$x = \frac{X}{L_0}\,,\ z = \frac{Z}{L_0}\,,\ u = \frac{U}{U_2}\,,\ w = \frac{W}{U_2},\ \psi = \frac{\Psi}{U_2 L_0}\,,\ p = \frac{P L_0}{\mu U_2}\,; \tag{2.5}$$

such that the fluid domain is given by

$$-1 \leqslant x \leqslant +1, \quad -A \leqslant z \leqslant +A\,, \tag{2.6}$$

where $A = H_0/L_0$ is the aspect ratio.

Boundary conditions include:

(i) no slip on upper and lower lids:

$$\left.\begin{aligned} \frac{\partial \psi}{\partial z} &= S,\ \frac{\partial \psi}{\partial x} = 0 \quad \text{on} \quad z = +A\,, \\ \frac{\partial \psi}{\partial z} &= 1,\ \frac{\partial \psi}{\partial x} = 0 \quad \text{on} \quad z = -A\,. \end{aligned}\right\} \tag{2.7}$$

(ii) zero shear stress and zero normal velocity on the free surfaces:

$$\frac{\partial^2 \psi}{\partial z^2} - \frac{\partial^2 \psi}{\partial x^2} = 0\,,\ \frac{\partial \psi}{\partial z} = 0 \ \text{ on } \ x = \pm 1\,. \tag{2.8}$$

Conditions (2.7) and (2.8) are equivalent to imposing ψ = constant = 0 on all four boundaries together with $\partial\psi/\partial z = S$ on $z = +A$, $\partial\psi/\partial z = 1$ on $z = -A$ and $\partial^2\psi/\partial x^2 = 0$ on $x = \pm 1$. The complete boundary value problem, given in figure 4(*a*), is much simpler than the associated lid-driven cavity problem addressed by Joseph & Sturges (1978) and Shankar (1993), since the 'natural' eigenfunctions of equation (2.4) are in this case real. The general solution satisfying conditions on $x = \pm 1$ can be written (Thompson 1992) as

$$\psi(x,z) = \sum_{n=1}^{\infty} \left\{ z(A_n e^{\beta_n z} + B_n e^{-\beta_n z}) + C_n e^{\beta_n z} + D_n e^{-\beta_n z} \right\} \cos(\beta_n x)\,, \tag{2.9}$$

where the β_n are real eigenvalues given by

$$\beta_n = (n - 1/2)\pi, \quad n = 1, 2, \ldots. \tag{2.10}$$

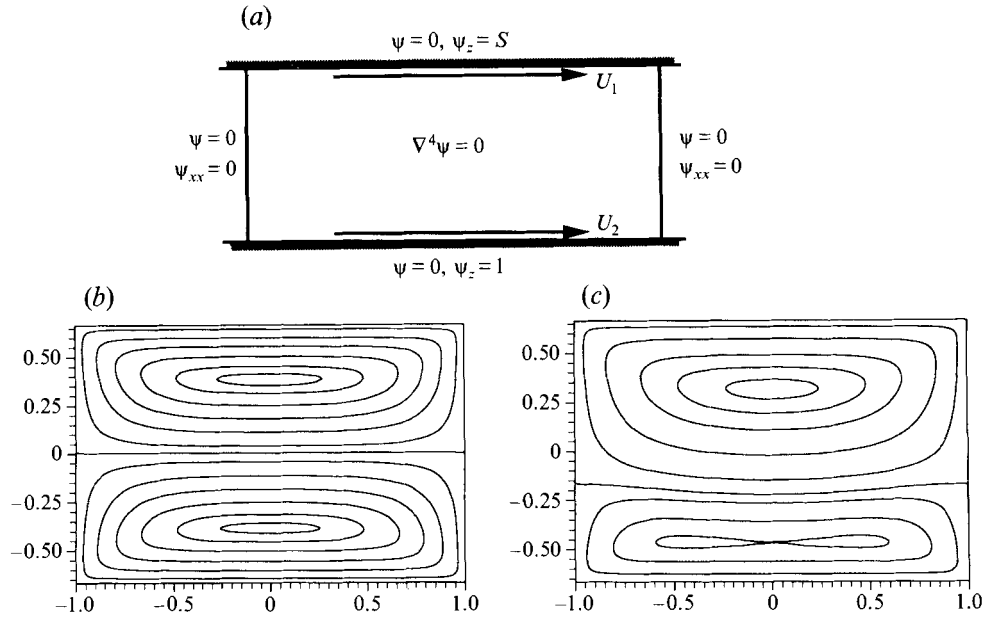

FIGURE 4. (*a*) Boundary conditions for Stokes flow in an idealized rectangular bead with zero flux, bounded by two free surfaces and two moving plates. Streamfunction solution of the zero flux model for (*b*) $A = 2/3$, $S = 1$, (*c*) $A = 2/3$, $S = 2$, illustrating the rich sub-structure that arises as a result of a stagnation point bifurcation.

The unknown coefficients A_n, B_n, C_n and D_n are determined from conditions on $z = \pm A$:

$$\left.\begin{aligned} A_n &= (-1)^{(n+1)} \frac{\left[e^{\beta_n A} - \dfrac{2A\beta_n}{\sinh 2\beta_n A} e^{-\beta_n A}\right] S - \left[e^{-\beta_n} - \dfrac{2A\beta_n}{\sinh 2\beta_n A} e^{\beta_n A}\right]}{\dfrac{\beta_n}{\sinh \beta_n A}\left[\sinh^2 2\beta_n A - 4\beta_n^2 A^2\right]}, \\ B_n &= (-1)^{(n+1)} \frac{\left[e^{\beta_n A} - \dfrac{2A\beta_n}{\sinh 2\beta_n A} e^{-\beta_n A}\right] - \left[e^{-\beta_n} - \dfrac{2A\beta_n}{\sinh 2\beta_n A} e^{\beta_n A}\right] S}{\dfrac{\beta_n}{\sinh \beta_n A}\left[\sinh^2 2\beta_n A - 4\beta_n^2 A^2\right]}, \\ C_n &= -A\left(\frac{A_n\left[\cosh 2\beta_n A\right] + B_n}{\cosh 2\beta_n A}\right), \\ D_n &= A\left(A_n\left[e^{-2\beta_n A} - e^{-\beta_n A}\right] + B_n\left[1 - \frac{e^{-\beta_n A}}{\cosh 2\beta_n A}\right]\right). \end{aligned}\right\} \quad (2.11)$$

The series given by equation (2.9) is truncated at the point where convergence is achieved. In practice 20 terms are found to be sufficient – experience shows that streamfunction values agree to six decimal places whether 20 or 50 terms are used in the series expansion (Thompson 1992).

Figure 4(*b*) shows streamline contours for the above problem first obtained by Thompson (1992). There is close agreement between the eddy structure observed

experimentally, figure 3(*a*), and the analytical prediction of figure 4(*b*). The flow is seen to exhibit a double-eddy structure with both eddies of equal size and separated by a dividing streamline.

Apart from the presence of eddies two, quite unexpected, results emerge from the zero flux model:

(i) As A is decreased or S is varied the eddies undergo a structural transformation. At a critical value, a stagnation point bifurcation arises – an eddy centre becomes a saddle point – so that what was once a single large eddy now consists of a separatrix with one saddle point, two sub-eddies with centres, and an outer circulation. This flow structure is demonstrated in figure 4(*c*) for the case $A = 2/3$, $S = 2$. The upper eddy is now twice the depth of the lower one, mirroring the global features observed experimentally, figure 3(*b*); work is currently being directed at improving the spatial resolution of experiments in order to reveal the underlying sub-structure. Similarly, stagnation point bifurcations in two-dimensional Stokes flows due to varying aspect ratio and speed ratio is the subject of further research.

(ii) In terms of the streamfunction, ψ, the width-wise pressure gradient, $\partial p/\partial x$, is given by

$$\frac{\partial p}{\partial x} = \nabla^2 u = \frac{\partial^3 \psi}{\partial z^3} + \frac{\partial^3 \psi}{\partial x^2 \partial z}\,, \tag{2.12}$$

or in series form as

$$\frac{\partial p}{\partial x} = 2\sum_{n=1}^{\infty} \beta_n^2 \left\{A_n e^{\beta_n z} + B_n e^{-\beta_n z}\right\} \cos(\beta_n x), \quad |z| \leqslant A, \quad |x| \leqslant 1\,. \tag{2.13}$$

In the central core of the flow domain, away from either meniscus, as S is varied for a given aspect ratio, A, $\partial p/\partial x$ is effectively constant on the centreline $z = 0$. This indicates a pressure profile linear in x which is in marked contrast to that observed in an inlet-flooded roll coater which exhibits a characteristic maximum and minimum (Pitts & Greiller 1961).

By integrating expression (2.13) fluid pressure is determined to within an arbitrary constant, whose value cannot be determined from this simple model since curvature of the menisci is neglected. Figure 5 shows p plotted along the centreline of the solution domain for two values of S and A. These were found by taking 20 terms in the series expansion for p whose convergence characteristics are the same as those for ψ. This linear pressure distribution suggests that the pressure field in a meniscus coater may be entirely sub-ambient arising as a result of capillary action at the upstream and downstream menisci. It is found (Thompson 1992), that for small aspect ratios, pressure is effectively independent of z – a result which forms the basis of the small flux model presented in §3.

3. Small flux model and lubrication solution

The key results from the zero flux model that, in the central core, the flow is one-dimensional and pressure is independent of Z suggest the need for a model which takes account of a small, non-zero flux and treats the velocity field as a combination of Couette and Poiseuille flow.

Figure 6 shows a schematic of the bead in the interval $-B \leqslant X \leqslant +D$. Fluid enters in a uniform layer of thickness H_i and exits by way of two uniform layers of thickness H_1 and H_2 attached to the web on the upper roll and the lower roll respectively.

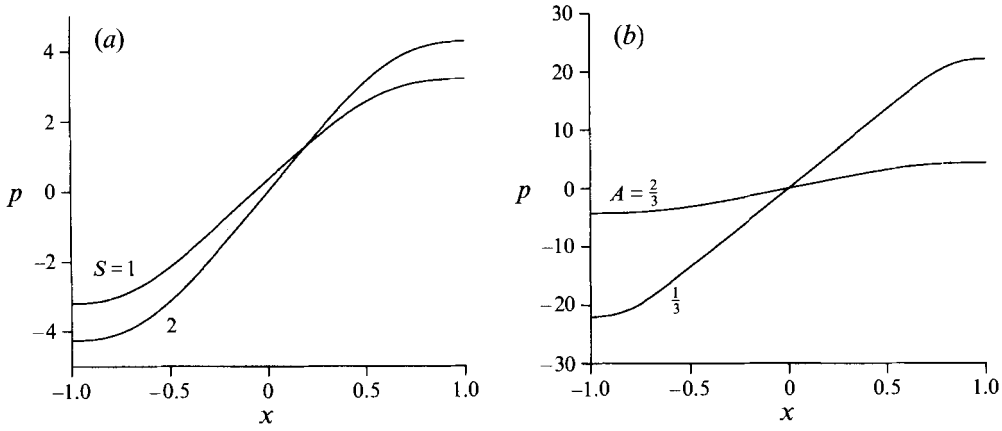

FIGURE 5. Width-wise pressure distribution as predicted by the zero flux model: (a) $A = 2/3$, $S = 1, 2$; (b) $S = 1$, $A = 2/3, 1/3$.

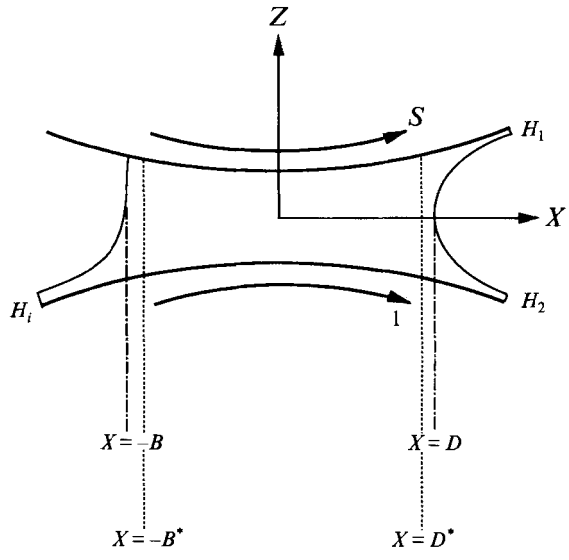

FIGURE 6. Schematic of a meniscus coating bead with small flux, bounded by two menisci and two moving rolls.

Continuity of flow requires that

$$H_i = H_2 + SH_1 . \tag{3.1}$$

Assuming lubrication theory to be valid (where the flow is effectively one-dimensional; $W/U \ll 1$ and $\partial/\partial X \ll \partial/\partial Z$), equations (2.1) reduce to

$$\left.\begin{aligned} \frac{\partial P}{\partial X} &= \mu \frac{\partial^2 U}{\partial Z^2} , \\ \frac{\partial P}{\partial Z} &= 0 , \end{aligned}\right\} \tag{3.2}$$

and the solution for velocity $U(X,Z)$ satisfying $U = U_1$ at $Z = H(X)$ and $U = U_2$

on $Z = -H(X)$ is

$$U = \frac{1}{2\mu}\frac{\partial P}{\partial X}(Z^2 - H^2) + \frac{(U_1 - U_2)}{2}\frac{Z}{H} + \frac{(U_1 + U_2)}{2}, \tag{3.3}$$

where $H(X)$ is the semi-gap width at station X, approximated by

$$H(X) = H_0 + \frac{X^2}{2R}, \tag{3.4}$$

with $2/R = 1/R_1 + 1/R_2$. The flux Q, per unit axial length, is given by

$$Q = \int_{-H}^{+H} U\mathrm{d}Z = -\frac{2}{3\mu}\frac{\mathrm{d}P}{\mathrm{d}X}H^3 + (U_1 + U_2)H, \tag{3.5}$$

and since classical roll coating (with flooded inlets) is a self-metered process – in which the flow rate Q is determined by geometry and roll speeds – it is usual to non-dimensionalize Q by means of an average speed $(U_1 + U_2)/2$ and the gap thickness $2H_0$, giving

$$\lambda = \frac{Q}{(U_1 + U_2)H_0}. \tag{3.6}$$

In meniscus roll coating, however, neither the gap nor the upper roll speed play any part in determining Q. In fact all the fluid approaching the inlet is transmitted through the nip and Q is given by

$$Q = U_2 H_i. \tag{3.7}$$

It is useful therefore to introduce a new dimensionless flow rate λ_2 defined by

$$\lambda_2 = \frac{Q}{U_2(2H_0)} = \frac{H_i}{2H_0}, \tag{3.8}$$

where λ_2 provides a natural measure of the degree of inlet starvation and is related to λ by

$$\lambda_2 = \frac{(1+S)}{2}\lambda, \tag{3.9}$$

such that $\lambda = \lambda_2$ when $S = 1$ only.

Reynolds' equation for pressure $P(X)$ follows from equations (3.5) and (3.6):

$$\frac{\mathrm{d}P}{\mathrm{d}X} = \frac{3\mu(U_1 + U_2)}{2H^2(X)}\left(1 - \frac{\lambda H_0}{H(X)}\right), \tag{3.10}$$

and hence the velocity $U(X,Z)$ can be written in the form

$$\frac{U(X,Z)}{U_2} = \frac{3(1+S)}{4}\left(1 - \frac{\lambda H_0}{H(X)}\right)\left(\frac{Z^2}{H^2(X)} - 1\right) + \left(\frac{S-1}{2}\right)\frac{Z}{H(X)} + \left(\frac{1+S}{2}\right). \tag{3.11}$$

Since a meniscus roll coater operates with $\lambda \ll 1$ then in the central core, where $H(X) \approx H_0$, the pressure gradient is a positive constant proportional to $\mu(1+S)/H_0^2$. Also, $U(X,Z)$ is quadratic in Z and has two zeros across the gap for all positive values of S. It can, therefore, adequately describe unidirectional flow in the central core consisting of a narrow transfer jet snaking around a pair of eddies. As indicated previously this jet is the means by which fluid is transferred to the web on the upper roll and, as such, is similar to that appearing in the upstream recirculation region of an inlet-flooded roll coater (Pearson 1985).

A suitable domain for this lubrication solution cannot extend as far as the free surfaces for obvious reasons. However, the W-component of velocity appears to be significant only in a very thin layer adjacent to each free surface. Hence we shall solve Reynolds' equation in the domain $-B^* \leqslant X \leqslant D^*$, as shown in figure 6, and also assume that fluid pressure at each end point is given by capillary pressure at the corresponding meniscus.

If R_B, R_D are the radii of curvature of the upstream and downstream menisci then the fluid pressures there are given by

$$P(X = -B^*) = -\frac{\sigma}{R_B}, \qquad P(X = D^*) = -\frac{\sigma}{R_D}, \tag{3.12}$$

where σ is surface tension.

Introducing the following non-dimensional variables:

$$\bar{x} = \frac{X}{(2RH_0)^{1/2}}; \quad \bar{z} = \frac{Z}{H_0}; \quad \bar{u} = \frac{U}{U_2}; \quad \bar{p} = \frac{2P}{\mu(U_1 + U_2)} \frac{H_0^2}{(2RH_0)^{1/2}}, \tag{3.13}$$

reduces Reynolds' equation (equation (3.10)) to the form

$$\frac{\mathrm{d}\bar{p}}{\mathrm{d}\bar{x}} = \frac{3}{(1+\bar{x}^2)^2}\left[1 - \frac{\lambda}{(1+\bar{x}^2)}\right], \tag{3.14}$$

which is solved for pressure by writing $\bar{x} = \tan\alpha$:

$$\bar{p}(\alpha) = 3\int(\cos^2\alpha - \lambda\cos^4\alpha)\mathrm{d}\alpha + \text{constant}. \tag{3.15}$$

Approximating R_D and R_B by the semi-gap width, $H(D)$, and the full gap width, $2H(B)$, respectively and writing $\bar{d} = D/(2RH_0)^{1/2}$; $\bar{b} = B/(2RH_0)^{1/2}$, then

$$H(D) = R_D = H_0(1 + \bar{d}^2), \qquad 2H(B) = R_B = H_0(1 + \bar{b}^2). \tag{3.16}$$

Hence the solution of (3.15) subject to (3.12) and (3.16) with $\bar{b} = \tan\alpha_b$, $\bar{d} = \tan\alpha_d$ and capillary number defined by

$$Ca = \frac{\mu(U_1 + U_2)}{2\sigma} = \frac{\mu U_2(1+S)}{2\sigma}, \tag{3.17}$$

is

$$\frac{\sqrt{2}}{3}\frac{(H_0/R)^{1/2}}{Ca}\left[\cos^2\alpha_b - 2\cos^2\alpha_d\right] = \left[\sin 2\alpha_b + \sin 2\alpha_d + 2\alpha_b + 2\alpha_d\right] - \lambda\left[\frac{\sin 4\alpha_b + \sin 4\alpha_d}{8} + \frac{3}{2}(\alpha_b + \alpha_d) + \sin 2\alpha_b + \sin 2\alpha_d\right]. \tag{3.18}$$

The two non-dimensional parameters appearing in equation (3.18) are flow rate λ and a modified capillary number, $Ca(R/H_0)^{1/2}$, which measures the relative importance of hydrodynamic to capillary pressure.

In the classical roll coating regime inlets are flooded, modified capillary numbers are large and the left-hand side of equation (3.18) is negligible. In the meniscus coating regime, however, flow rates are small $\lambda \ll 1$, $Ca(R/H_0)^{1/2} \ll 1$ and so the left-hand side of (3.18) is of similar magnitude to the first term on the right-hand side. This indicates that hydrodynamic pressures in the fluid bead are of similar magnitude to the capillary pressure generated at the upstream meniscus.

Once $Ca, (R/H_0)^{1/2}$ and λ are specified, then equation (3.18) yields a relation

between α_b and α_d which has predictive value provided either α_b or α_d can be determined independently. In fact α_d can be estimated using the results of Landau & Levich (1942) relating the uniform film thicknesses on the web and lower roll to the radius of curvature, R_D, of the downstream meniscus:

$$\frac{H_1}{R_D} = 1.34\left(\frac{\mu U_1}{\sigma}\right)^{2/3}, \qquad \frac{H_2}{R_D} = 1.34\left(\frac{\mu U_2}{\sigma}\right)^{2/3}. \tag{3.19}$$

Taking expression (3.16) as a suitable approximation for R_D the following results arise.

(i) For the symmetric case of equal speed rolling $U_1 = U_2 = U$, $S = 1$, $\lambda = \lambda_2$, $Ca = \mu U/\sigma$, $H_1 = H_2 = H_i/2$ and equations (3.16) and (3.19) give

$$1 + \bar{d}^2 = \sec^2\alpha_d = \frac{\lambda_2}{1.34(Ca)^{2/3}}. \tag{3.20}$$

For a given flow rate equation (3.20) is solved for α_d as a function of capillary number. This solution is then used to solve equation (3.18) for α_b as a function of capillary number once the geometry ratio, R/H_0, is specified. Figure 7(*a*) shows plots of $\tan\alpha$ against Ca for $R/H_0 = 100$ and $\lambda_2 = 0.2$ in which the upper and lower curves represent the location of the downstream and upstream menisci, respectively.

For the asymmetric case, $S \neq 1, \lambda \neq \lambda_2$, and expressions for H_1 and H_2 given by (3.19) are substituted into equation (3.1) to give

$$1.34R_D\left[S\left(\frac{\mu U_1}{\sigma}\right)^{2/3} + \left(\frac{\mu U_2}{\sigma}\right)^{2/3}\right] = H_i, \tag{3.21}$$

which can be rearranged using the identities

$$U_2 = \left(\frac{U_1 + U_2}{2}\right)\left(\frac{2}{1+S}\right) \quad \text{and} \quad U_1 = \left(\frac{U_1 + U_2}{2}\right)\left(\frac{2S}{1+S}\right),$$

to yield an expression for $\bar{d}$:

$$1 + \bar{d}^2 = \frac{2\lambda_2}{1.34(Ca)^{2/3}} \frac{\left(\frac{1}{2}(1+S)\right)^{2/3}}{\left[1 + S^{2/3}\right]}. \tag{3.22}$$

With R/H_0, λ_2 and S specified, equations (3.22) and (3.18) are solved for α_d and α_b as functions of capillary number thus giving plots of $\tan\alpha$ against Ca for the asymmetric flow, $S = 1/2$, when $R/H_0 = 100$ and $\lambda_2 = 0.2$, figure 7(*a*).

The speed ratio clearly has a negligible effect on the position of the upstream and downstream free surfaces. It is a result observed experimentally (Malone 1992), and to be expected in the light of equation (3.22) where the factor $[(1+S)/2]^{2/3}/[1+S^{2/3}]$ is symmetric about $S = 1$ and has only a 6% variation over the range of practical interest, $1/5 < S < 5$.

(ii) Since speed ratio has a negligible effect then, for a given flow rate, it follows that capillary number determines the position of the downstream meniscus whereas the upstream meniscus is determined by both capillary number and the modified capillary number, $Ca(R/H_0)^{1/2}$, equation (3.18). This is illustrated in figure 7(*b*) where curves are shown for symmetric flows with $R/H_0 = 100$, 200 and 400.

(iii) Figure 7(*a*,*b*) illustrates that a fluid bead is established with the upstream meniscus in the interval $0 < \bar{b} < 2$ provided that the capillary number lies in the range $10^{-3} < Ca < 10^{-2}$.

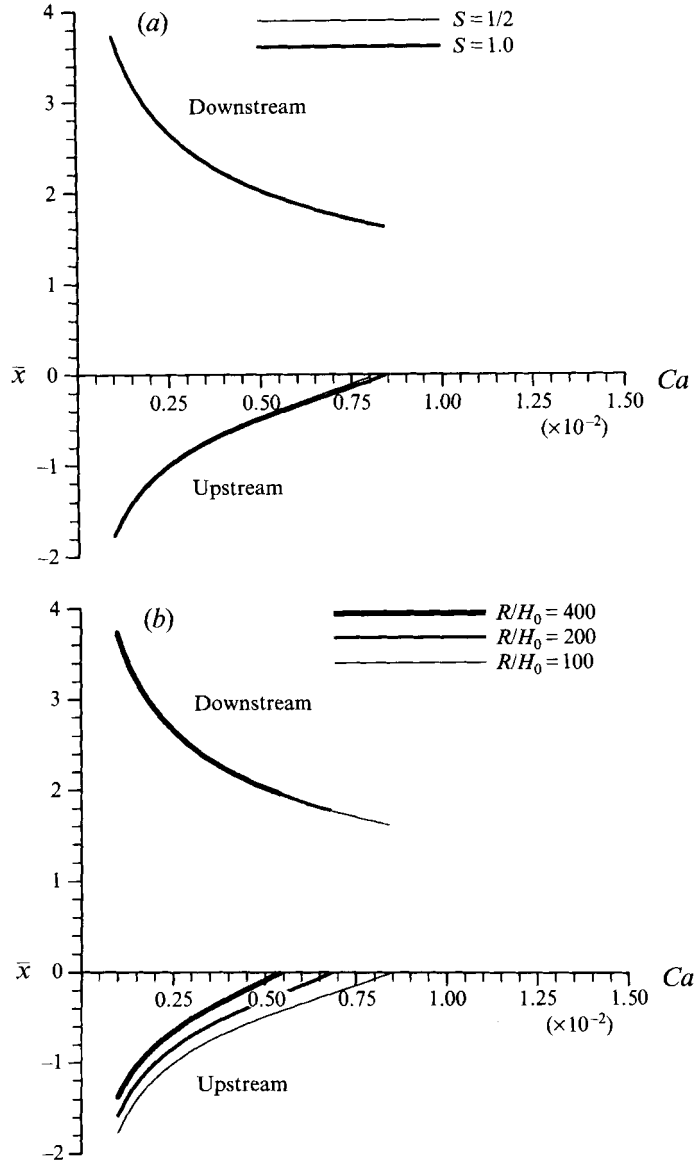

FIGURE 7. (*a*) Upstream and downstream meniscus locations plotted as a function of capillary number for the case $R/H_0 = 100$, $\lambda_2 = 0.2$ with $S = 1/2$ and $S = 1$. (*b*) Curves showing the effect of R/H_0 on the position of the upstream meniscus.

For a given R/H_0, it is observed that $\bar{b}$ decreases as Ca increases and so the upstream meniscus approaches and eventually passes through the nip. Once through the nip the interface appears to become unstable (Malone 1992), giving rise to a phenomenon called 'bead break' – the cause of which is unclear and the subject of further investigation. On the other hand, when Ca is decreased the upstream meniscus moves away from the nip yet, in practice, it can only move out so far. At a certain distance capillary pressure is comparable to that at the downstream meniscus and the pressure field 'collapses'. The assumption on which the small flux model is based – that pressure and viscous forces are in balance, with inertia negligible – is no longer valid and therefore a stable bead cannot form. Computational results, described in

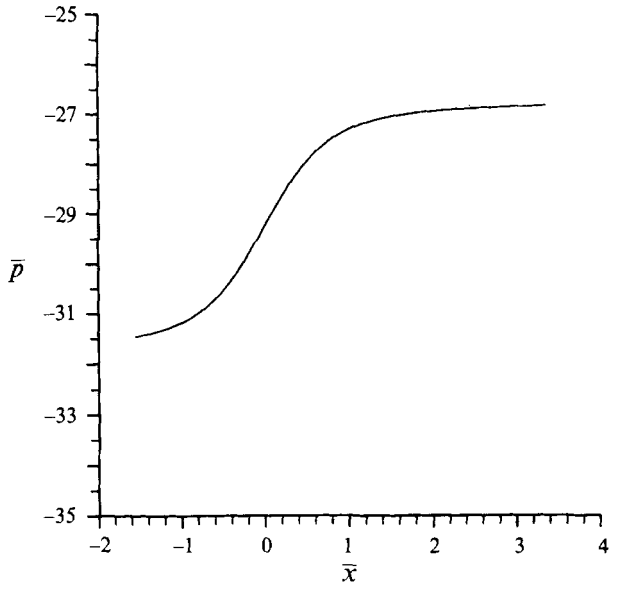

FIGURE 8. A non-dimensional pressure profile for $R/H_0 = 100, Ca = 1.3 \times 10^{-3}$, $S = 1$, $\lambda = 0.075$, $\bar{b} = 1.55$ and $\bar{d} = 3.5$ as predicted via the small flux model.

the following section, confirm that the location of the upstream meniscus usually lies in the range $0 < \bar{b} < 2$. Figure 7(*a*,*b*) also indicates that the extent of the fluid bead should decrease monotonically with capillary number.

(iv) Figure 8 shows a typical pressure distribution, as predicted by the small flux model for $S = 1$, $\lambda = 0.075$, $R/H_0 = 100$, $Ca = 1.3 \times 10^{-3}$, $\bar{b} = \tan\alpha_b = 1.55$ and $\bar{d} = \tan\alpha_d = 3.5$. As expected this pressure field is sub-ambient entirely as a result of capillary action at the menisci and exhibits a linear rise through the central core as predicted by the zero flux model.

(v) Conditions (3.12) and (3.19) are the boundary conditions required to close the problem and as such have a similar status to those derived by Coyne & Elrod (1970). Ruschak (1982) compared finite element results for flow rate against capillary number with those predicted using Coyne & Elrod's conditions, showing very close agreement for capillary numbers greater than 10^{-2}. Later, Ruschak (1985), derived a two-thirds power law for film thickness ratio:

$$\frac{H_1}{H_2} = S^{2/3}, \tag{3.23}$$

a result which was shown to be asymptotically valid as $Ca \longrightarrow 0$. Hence one would expect expression (3.19) to be particularly applicable to meniscus coating where $Ca < 10^{-2}$. Indeed, in the following section computational results are seen to be in accord with equation (3.23).

4. Small flux model and finite element solutions

Further refinements to the mathematical model include the presence of curved menisci, nonlinear free-surface boundary conditions and a dynamic contact line requiring the imposition of a slip-length and apparent contact angle, the latter suggested by experiment. This requires the solution of the full nonlinear boundary

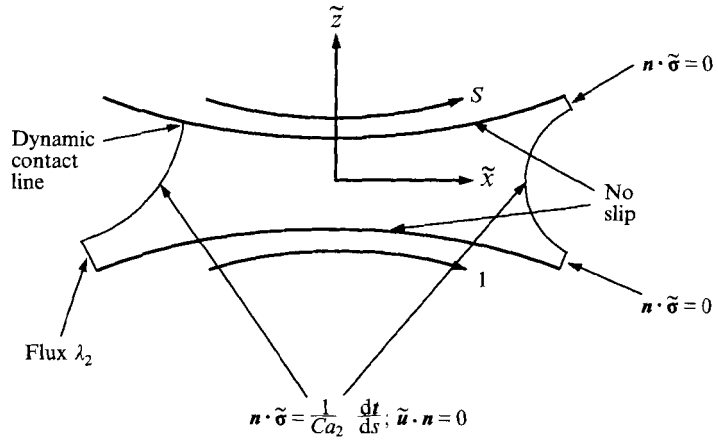

FIGURE 9. Nonlinear boundary conditions for Stokes flow in a bead incorporating the effects of a dynamic contact line and curved menisci: n and t are unit normal and tangent vectors, respectively, and s is the free surface arc-length.

value problem described by equations (2.1) and (2.2) written in divergence form (Kistler & Scriven 1983), as

$$\nabla\cdot\boldsymbol{T} = 0\,, \qquad \nabla\cdot\boldsymbol{U} = 0\,, \tag{4.1}$$

where $\boldsymbol{T} = -P\boldsymbol{I} + \mu[\nabla\,\boldsymbol{U} + (\nabla\,\boldsymbol{U})^T]$ and $\boldsymbol{I}$ are the stress and unit tensor, respectively.

A numerical solution was obtained using a Galerkin, weighted residual finite element formulation for equations (4.1), with X, Z, U, W, P and $\boldsymbol{T}$ non-dimensionalized as follows:

$$\tilde{x} = \frac{X}{H_0};\ \tilde{z} = \frac{Z}{H_0};\ \tilde{u} = \frac{U}{U_2};\ \tilde{w} = \frac{W}{U_2};\ \tilde{p} = \frac{PH_0}{\mu U_2};\ \tilde{\boldsymbol{\sigma}} = \frac{\boldsymbol{T}H_0}{\mu U_2}. \tag{4.2}$$

The attendant boundary conditions are given in figure 9. The reader will note that the capillary number in this case is defined as $Ca_2 = \mu U_2/\sigma$ and is related to Ca in the following way: $Ca = [(1+S)/2]/Ca_2$.

A finite element approach was adopted because of its topological flexibility, particularly in relation to flows bounded by one, or more, highly curved free surfaces which can be handled satisfactorily with an appropriately formulated parametric representation. In the current work the spine approach of Kistler & Scriven (1983) is adopted, together with a novel combination of multiple origins and spine interdependency (Gaskell *et al.* 1995), as a more cost effective alternative to employing elliptic grid generation (Christodoulou & Scriven 1992), within an iterative framework, for the same element density.

The region of interest was tessellated into triangular V6/P3 elements, which are taken to satisfy the LBB stability condition (Babuska & Aziz 1972). With the pressure interpolation one order lower than that for velocity, the rate of convergence is 'optimal' and no 'locking' (Hughes 1987), occurs. The assembled global stiffness matrix was solved using the frontal method (Hood 1976), and Newton iteration, resulting in second-order convergence of the system, within a maximum of six iterations.

The grid-independence of the solutions, in particular the accuracy of predicted film thicknesses, was investigated by employing systematic grid refinement of the solution domain. Four levels of grid refinement were considered containing 549, 1615, 3185, 8241 elements and 2562, 7330, 14399, 37143 degrees of freedom, respectively. Results for the latter two grid levels were found to be indistinguishable and hence

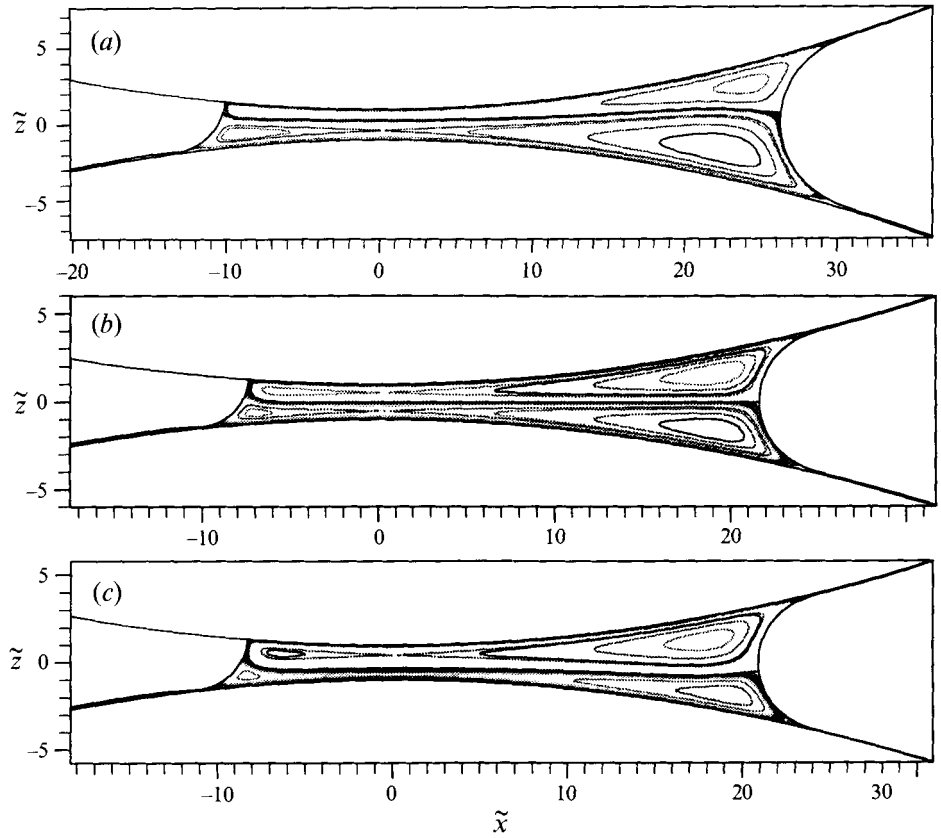

FIGURE 10. Flow structures in the bead of a meniscus roll coater for $R/H_0 = 100$ and $\lambda_2 = 0.075$: (*a*) $S = 1/2$, $Ca_2 = 2.25 \times 10^{-3}$; (*b*) $S = 1$, $Ca_2 = 1.80 \times 10^{-3}$; (*c*) $S = 2$, $Ca_2 = 7.0 \times 10^{-4}$.

a grid containing 3185 elements was deemed adequate to guarantee fully converged, grid-independent solutions.

Finite element solutions were found for a two-roll coater with $R/H_0 = 100$, a constant flow rate $\lambda_2 = 0.075$, various capillary numbers, Ca_2, and an apparent contact angle of 95° at the dynamic wetting line, as suggested from experiment (R. C. Lodge 1994, personal communication). Figure 10(*a–c*) shows streamline plots of the flow when $S = 1/2$, 1 and 2 with corresponding capillary numbers $Ca_2 = 2.25 \times 10^{-3}$, 1.8×10^{-3} and 7.0×10^{-4}, respectively.

Figure 10 reveals a 'double-eddy' structure with eddy thickness dependent on S – in qualitative agreement with experiment and the predictions of the zero flux model. The flux of fluid in the transfer jet, subsequently referred to as the 'primary snake', is seen to increase with S. Corresponding sub-ambient pressure fields are displayed in figure 11 which are in accord with the predictions from the small flux model. Figure 12 shows the effect of flow rate λ_2 on film thickness ratio for S in the interval $1/5 < S < 5/2$, illustrating that H_1/H_2 is independent of λ_2. Figure 13, on the other hand, shows the variation of H_1/H_2 with S for a flow rate $\lambda_2 = 0.14$, including a comparison with equation (3.23) obtained from the analysis of Landau & Levich, equation (3.19). Agreement between the two curves is extremely good over the whole speed ratio range.

For a non-dimensional flow rate $\lambda_2 = 0.2$ and gap ratio, $R/H_0 = 100$, figure 14 shows comparisons between finite element solutions and analytical results via the

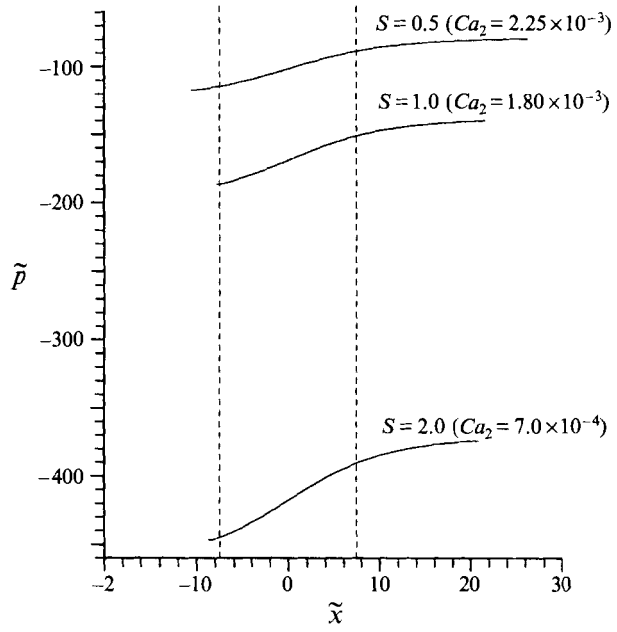

FIGURE 11. Pressure distributions, taken along the centreline, $\tilde{z} = 0$, for $R/H_0 = 100$, $\lambda_2 = 0.075$ and corresponding to each of the flows in figure 10.

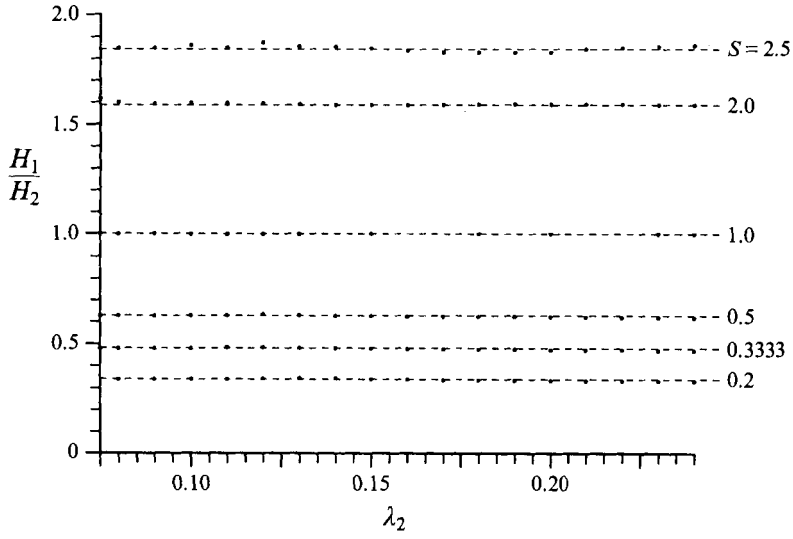

FIGURE 12. The effect of flow rate, λ_2, on film thickness ratio, H_1/H_2, for $R/H_0 = 100$ and S in the interval $1/5 < S < 5/2$: •, finite element solutions; - - - -, Landau–Levich, equation (3.19).

small flux model for two values of S. Agreement is surprisingly good and shows each meniscus approaching the nip as Ca increases, so that the extent of the fluid bead diminishes.

In order to assess the significance of the gap ratio R/H_0, equations (3.18) and (3.20) are of particular relevance. With flow rate specified, equation (3.20) implies that Ca determines the position of the downstream meniscus and, whatever its value, equation (3.18) implies that the modified capillary number , $Ca(R/H_0)^{1/2}$, is the key parameter

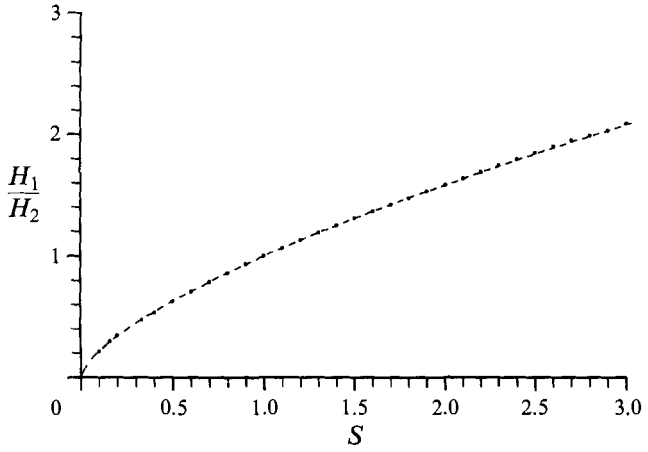

FIGURE 13. The variation of H_1/H_2 with S for $R/H_0 = 100$ and flow rate, $\lambda_2 = 0.14$: •, finite element solutions; - - - - -, Landau–Levich, equation (3.19).

responsible for determining the position of the upstream meniscus. This suggests that a plot of $Ca(R/H_0)^{1/2}$ against B/H_0 may serve to identify that part of parameter space in which meniscus roll coating arises. Hence figure 15 includes the relevant finite element solutions for $\lambda_2 = 0.2$ and S in the interval $1/5 < S < 3$. Meniscus roll coating is therefore revealed to be a process arising under conditions of both small capillary number and small modified capillary number; $Ca(R/H_0)^{1/2} \lesssim 0.15$.

5. Feed condition and critical flow rates

In this section the effect is considered of varying the non-dimensional flux λ, or feed condition, and three critical flow rates are identified.

5.1. *Pressure field transformation ($\lambda = 1$)*

First it is shown that $\lambda < 1$ is a necessary condition for obtaining pressure profiles typical of meniscus roll coating. If the feed condition is such that the inlet is flooded or moderately starved then the pressure profile will exhibit stationary points where pressure has either a local maximum or minimum value. At a stationary point $\mathrm{d}\tilde{p}/\mathrm{d}\tilde{x} = 0$ and therefore this condition together with Reynolds' equation for pressure, equation (3.10), reveals their locations to be where

$$\tilde{x}^2 = \lambda - 1 . \tag{5.1}$$

Provided $\lambda > 1$ these stationary points will be located symmetrically about the nip. When $\lambda < 1$, equation (5.1) has no real solutions and therefore no stationary points occur. Hence $\lambda = 1$ is the critical flow rate at which there is a smooth transformation in the shape of the pressure profile to one which exhibits no stationary points, is everywhere sub-ambient and is dominated by capillary action at the menisci. Furthermore, computational results have confirmed that this flow rate is independent of Ca, S and R/H_0. Figure 16 shows the pressure profile transformation with λ in the interval $0.8 < \lambda < 1.3$, obtained using the finite element method with $R/H_0 = 100$ and $S = 1$.

5.2. *Effect of feed condition on velocity field*

Clearly $\lambda < 1$ is only a necessary condition for meniscus roll coating since, in practice,

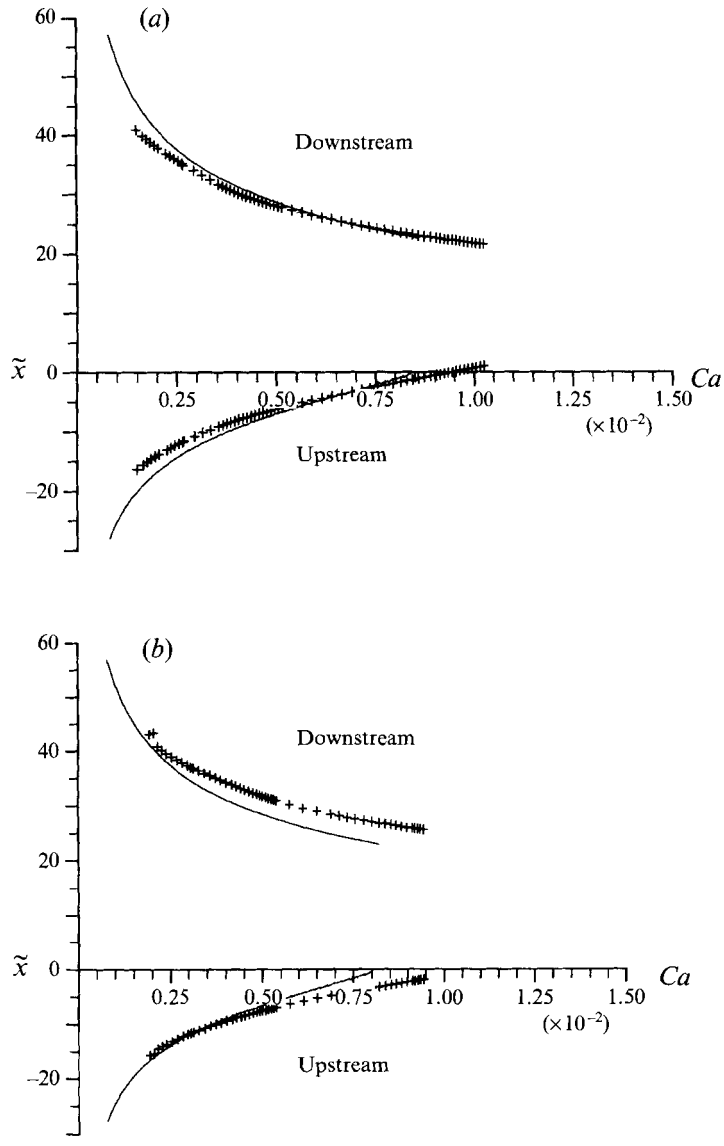

FIGURE 14. A comparison between analytical and finite element solutions (+) for the upstream and downstream meniscus locations as functions of Ca with $R/H_0 = 100$ and $\lambda_2 = 0.2$: (*a*) $S = 1$; (*b*) $S = 1/2$.

inlets are starved with $\lambda \ll 1$. To specify this coating regime more accurately requires additional information about the velocity field from the finite element solutions as the flow rate is varied.

Starting with an ultra-starved inlet, $\lambda_2 = 0.075$, figure 10(*a–c*) shows two large eddies and a characteristic primary snake carrying fluid to the web on the upper roll. From insight gained in §2 each eddy is seen to consist of a bounding streamline pinned to a free surface, an outer recirculation, a separatrix with one saddle point and two sub-eddies as illustrated in figure 17 for $S = 1/2$. As flow rate is increased gradually the additional flux causes pinching of the lower eddy close to the nip so that streamlines in its outer recirculation, including the bounding streamline, are drawn successively into the saddle point.

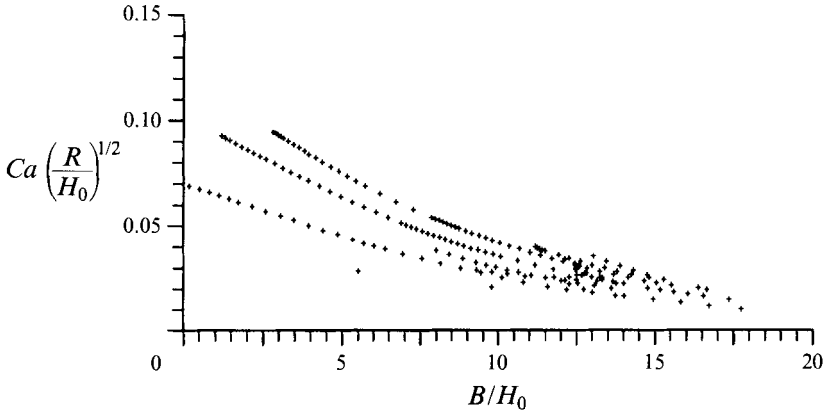

FIGURE 15. $Ca(R/H_0)^{1/2}$ plotted against B/H_0 obtained from finite element solutions with S in the interval $1/5 < S < 3$.

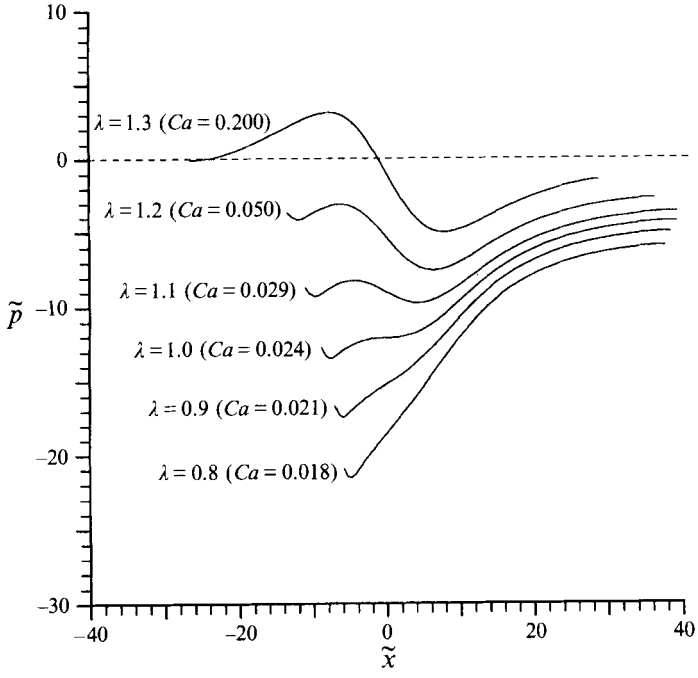

FIGURE 16. Pressure profiles for $R/H_0 = 100$, $S = 1$ and λ in the interval $0.8 < \lambda < 1.3$ illustrating the transformation in shape at $\lambda = 1$.

Figure 18(a) shows a flow pattern for a critical flow rate, $\lambda_{2s} = 0.1111$, $S = 1$, at which the bounding streamline is also part of the separatrix passing through three stagnation points P_1, P_2 and P_3. Also shown, located immediately below this separatrix, is a streamline (part of the primary snake) which will be next to be drawn into the saddle as λ_2 is increased. Figure 18(b) shows this streamline as part of the separatrix and the former separatrix/bounding streamline is now detached from the saddle point giving rise to a 'secondary snake' in the lower left of the diagram, that is fluid is able to circumnavigate the now isolated sub-eddy and flow between its bounding streamline $P_2P_3P_1$ and the separatrix. Fluid entering the bead can now transfer to the web on the upper roll via either the primary or secondary snakes.

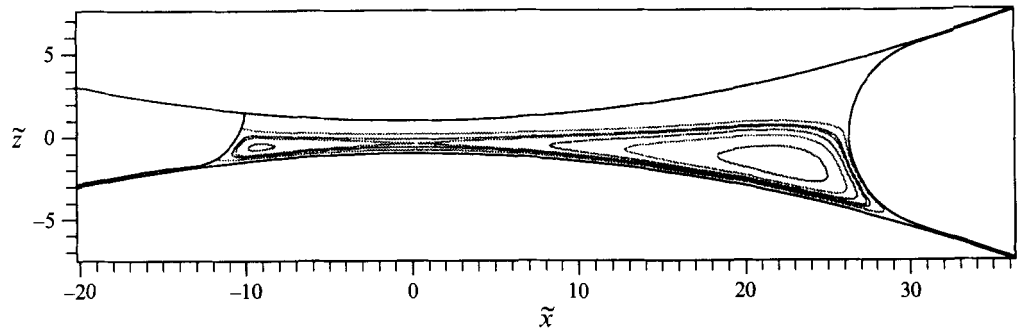

FIGURE 17. An illustration of the important streamlines and features which make up the 'lower eddy' for $R/H_0 = 100$, $Ca_2 = 2.25 \times 10^{-3}$, $\lambda_2 = 0.075$ and $S = 1/2$.

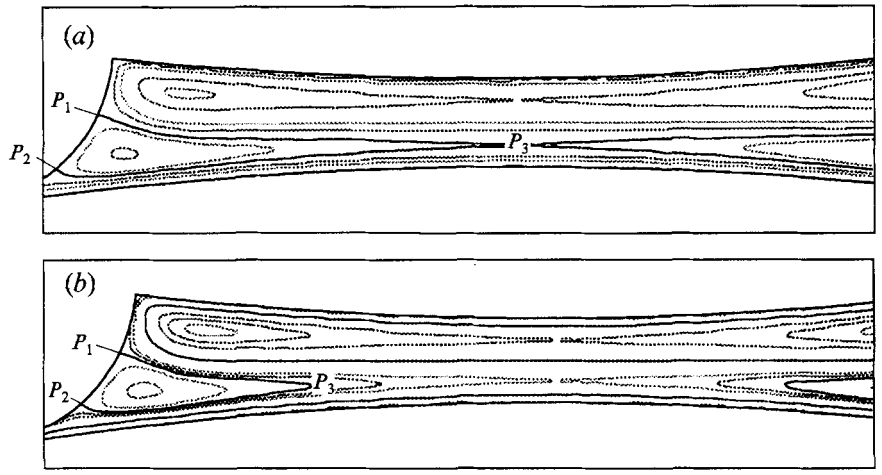

FIGURE 18. The onset of the secondary snake for $R/H_0 = 100$, $Ca_2 = 2 \times 10^{-3}$ and $S = 1$: (*a*) critical flow rate, $\lambda_2 = \lambda_{2s} = 0.1111$, in which part of the separatrix passes through the three stagnation points P_1, P_2, P_3; (*b*) the secondary snake is established, $\lambda_2 = 0.13$ and the bounding streamline $P_1P_2P_3$ is now detached from the saddle point.

As flow rate continues to increase, the flux in the secondary snake increases while that in the primary snake diminishes as streamlines are successively drawn into the saddle point. Also the lower left sub-eddy is observed to contract and disappear eventually, figure 19(*a,b*). A further critical flow rate now arises, $\lambda_{2p} = 0.3327$, when the flow in the primary snake decreases to zero; the primary snake disappears and fluid transfer to the web on the upper roll is entirely by means of a fully developed secondary snake. The critical flow pattern is illustrated in figure 20 where the dividing streamline, separating inlet fluid which reaches the web from that which remains attached to the lower roll, rises and is attracted into the saddle point.

Lubrication theory is used below to predict these two critical flow rates and requires the location of the lower of the two stagnation (saddle) points in the nip at $\tilde{x} = 0$. Its non-dimensional $\tilde{z}$ coordinate, $\tilde{z}_1$, is obtained as a function of λ and S via equation (3.11):

$$(1-\lambda)(\tilde{z}_1^2 - 1) + \frac{2}{3}\left(\frac{S-1}{S+1}\right)\tilde{z}_1 + \frac{2}{3} = 0\,. \tag{5.2}$$

Emergence of the secondary snake, $\lambda = \lambda_s$

When the flow conditions are critical with the secondary snake about to emerge,

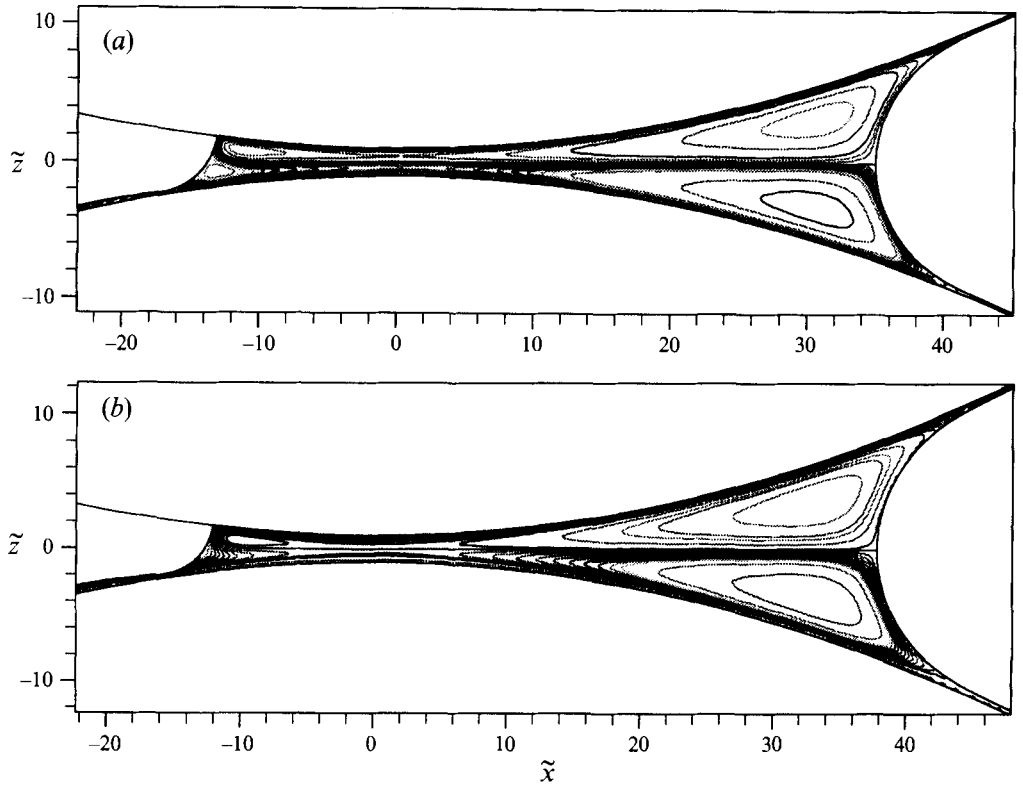

FIGURE 19. The effect of increasing the flux for $R/H_0 = 100$ and $S = 1$, showing that flux in the secondary snake increases while that in the primary snake diminishes: (*a*) $\lambda_2 = 0.18$, $Ca_2 = 2 \times 10^{-3}$; (*b*) $\lambda_2 = 0.3$, $Ca_2 = 3.25 \times 10^{-3}$.

$\lambda = \lambda_s$ and the total inlet flux, $Q = U_2 H_i$, is identically equal to the flux of fluid flowing between the lower roll and the lower of the two saddle points, figure 18(*a*). Hence evaluating the flux integral at $\tilde{x} = 0$:

$$\left.\begin{aligned} Q = U_2 H_i = U_2 H_0 (1+S)\lambda_s &= \int_{-H_0}^{Z_1} U(0,Z)\mathrm{d}Z \ , \\ \text{i.e.} \qquad (1+S)\lambda_s &= \int_{-1}^{\tilde{z}_1} \tilde{u}(0,\tilde{z})\mathrm{d}\tilde{z}, \end{aligned}\right\} \tag{5.3}$$

yields a cubic for $\tilde{z}_1$, now a function of λ_s and S:

$$\frac{3}{4}(1-\lambda_s)\left[\frac{\tilde{z}_1^3}{3} - \tilde{z}_1 - \frac{2}{3}\right] + \frac{(S-1)}{(S+1)}\frac{(\tilde{z}_1^2-1)}{4} + \frac{\tilde{z}_1+1}{2} = \lambda_s \ . \tag{5.4}$$

Solving equations (5.2) and (5.4) simultaneously gives the following solutions for $\tilde{z}_1$ and λ_s:

$$\tilde{z}_1 = \frac{[3(1-\lambda_s)(3\lambda_s(1+S)-(1-S))-(1-S)](1+S)}{3(1-\lambda_s)(3\lambda_s-1)(1+S)^2-(1-S)^2} \ , \tag{5.5}$$

$$\lambda_s = \frac{2}{9}\left[\frac{3+2S-2(S^2+3S)^{1/2}}{1+S}\right] \ . \tag{5.6}$$

This critical flow rate, λ_s, is speed-ratio dependent yet independent of capillary

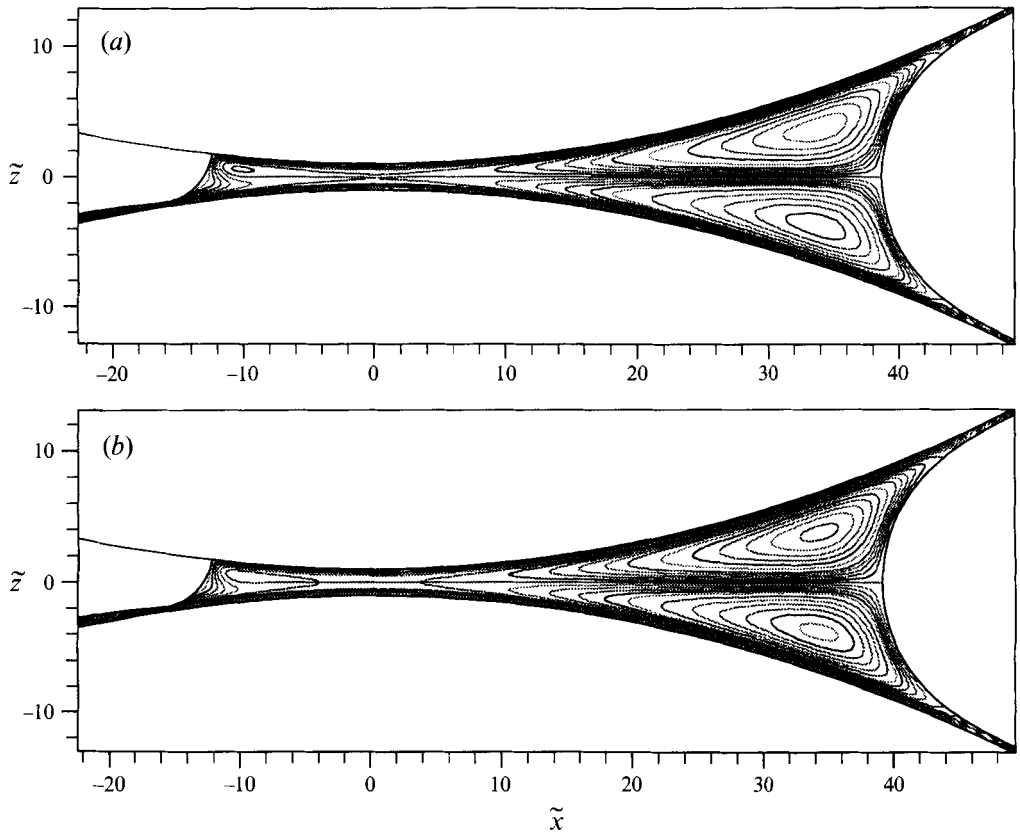

FIGURE 20. Switching off the primary snake when $R/H_0 = 100$ and $S = 1$: (*a*) critical flow rate $\lambda_2 = \lambda_{2p} = 0.3327$, $Ca_2 = 3.25 \times 10^{-3}$; (*b*) $\lambda_2 = 0.35$, $Ca_2 = 3.6 \times 10^{-3}$, fluid transfer to the web on the upper roll is entirely via the secondary snake and the saddle points have now moved apart.

number and geometry ratio. Figure 21 shows a plot of λ_s against S as given by equation (5.6) together with a number of data points for the onset of the secondary snake obtained via the finite element method. In particular, equation (5.6) predicts a critical flow rate of $\lambda_s = 1/9$ for symmetric flows ($S = 1$) which compares very favourably with the value of $\lambda_{2s} = 0.1111$ found computationally, see figure 18(*a*).

Disappearance of the primary-snake, $\lambda = \lambda_p$

The starting point is to consider the non-dimensional flux of the fluid between the lower roll and the lower of the two stagnation (saddle) points, evaluated at $\tilde{x} = 0$:

$$\int_{-1}^{\tilde{z}_1} \tilde{u}(0, \tilde{z}) \mathrm{d}\tilde{z} \,. \tag{5.7}$$

When conditions become critical (figure 20) $\lambda = \lambda_p$, the flux in the primary snake decreases to zero and the above flux is all carried away on the lower roll. This flux, given by expression (5.7) with $\lambda = \lambda_p$, is identically $U_2 H_2$; also

$$\frac{3}{4}(1-\lambda_p)\left[\frac{\tilde{z}_1^2}{3} - \tilde{z}_1 - \frac{2}{3}\right] + \frac{(S-1)}{(S+1)}\left(\frac{\tilde{z}_1^2 - 1}{4}\right) + \frac{(\tilde{z}_1 + 1)}{2} = \frac{H_2}{2H_0(1+S)} \,. \tag{5.8}$$

Solving equations (5.2) with $\lambda = \lambda_p$ and (5.8) will, in principle, determine $\tilde{z}_1$ and λ_p. The problem is that we do not have a general expression for H_2 except for the particular case of equal speed rolling, $S = 1$, for which $H_2/[2H_0(1+S)] = \frac{1}{2}\lambda_p$. This

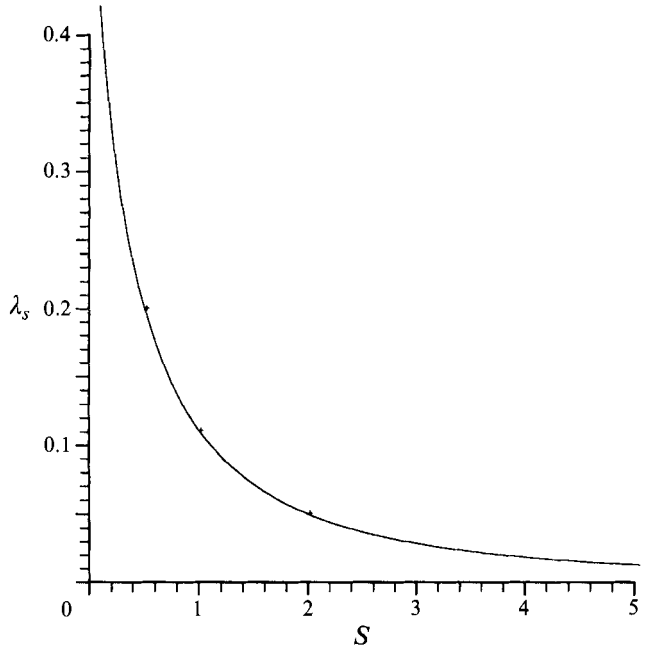

FIGURE 21. The onset of the secondary snake for $R/H_0 = 100$. Theoretical curve for critical flow rate λ_s as a function of S: •, data points obtained from finite element solutions; the curve is that predicted via lubrication theory, equation (5.6).

Inlet condition	Fluid transfer mechanism	Flow rate
Ultra-starved	Primary snake	$\lambda \leqslant \lambda_s$
Starved	Primary and secondary snakes	$\lambda_s < \lambda \ll \lambda_p < 1$

TABLE 1. The meniscus coating regime

is the only case for which λ_p can be predicted and the solutions are

$$\tilde{z}_1 = 0; \qquad \lambda_p = \tfrac{1}{3}\,. \tag{5.9}$$

The finite element computations yield a value of $\lambda_{2p} = 0.3327$ for this critical flow rate confirming once again the ability of lubrication theory to predict important features accurately. For unequal speeds λ_p has to be found computationally.

This critical flow rate, λ_p, signals the disappearance of the primary snake and hence fluid transfer to the web on the upper roll is by means of the secondary snake entirely. It also marks the decoupling of the upstream and downstream eddy structures, and termination of the meniscus coating regime.

5.3. *The meniscus coating regime*

In summary the previous results indicate that meniscus roll coating is an inlet-starved process, $\lambda \ll 1$, which can arise when the modified capillary number, $Ca(R/H_0)^{1/2} \lesssim 0.15$. Furthermore, it is useful to distinguish between two distinct conditions of inlet according to the fluid transfer mechanism. If the inlet is ultra-starved, $\lambda < \lambda_s \ll 1$, fluid is transferred only via the primary-snake; whereas if the inlet is starved, $\lambda_s < \lambda \ll \lambda_p$,

fluid is transferred by both the primary and secondary snakes. This distinction is summarized in table 1.

Finally the results presented in figures 10–21 reveal the many diverse features of meniscus roll coating. There is clearly a need for experimental validation of the complex eddy structures, pressure profiles, film thickness behaviour, meniscus locations and bead width.

The authors wish to acknowledge the continued support of ICI for this work and in particular Drs S. Abbott and S. Howe for bringing such a novel problem to their attention. H. M. Thompson would like to record his gratitude to the EPSRC for the provision of a studentship.

REFERENCES

BABUSKA, I. & AZIZ, A. K. 1972 Lectures on the mathematical foundations of the finite element method. In *Mathematical Foundations of the Finite Element Method with Applications to Partial Differential Equations* (ed. A. K. Aziz). Academic.

BENKREIRA, H., EDWARDS, M. F. & WILKINSON, W. L. 1981 Roll coating of purely viscous liquids. *Chem. Engng Sci.* **36**, 429–434.

BURLEY, R. & KENNEDY, B. S. 1976 An experimental study of air entrainment at a solid/liquid/gas interface. *Chem. Engng Sci.* **31**, 901–911.

CANEDO, E. L. & DENSON, C. D. 1989 Flows in driven cavities with a free surface *AIChE J.* **35**, 129.

CHRISTODOULOU, K. N. & SCRIVEN, L. E. 1992 Discretization of free surface flows and other moving boundary value problems *J. Comput. Phys.* **99**, 39–55.

COYLE, D. J. 1992 Roll coating. In *Modern Coating and Drying Technology* (ed. E. Cohen & E. Gutoff). VCH Publishers, New York.

COYLE, D. J., MACOSKO, C. W. & SCRIVEN, L. E. 1986 Film-splitting flows in forward roll coating. *J. Fluid Mech.* **171**, 183–207.

COYLE, D. J., MACOSKO, C. W. & SCRIVEN, L. E. 1987 Film-splitting flows of shear-thinning in forward roll coating flows. *AIChE J.*, **33**, 741–746.

COYLE, D. J., MACOSKO, C. W. & SCRIVEN, L. E. 1990*a* Stability of symmetric film splitting between counter rotating cylinders. *J. Fluid Mech.* **216**, 437–458.

COYLE, D. J., MACOSKO, C. W. & SCRIVEN, L. E. 1990*b* The fluid dynamics of reverse roll coating *AIChE J.* **36**, 161–174.

COYNE, J. C. & ELROD, H. G. 1970 Conditions for the rupture of a lubricating film. Part I: theoretical model. *J. Lub. Technol.* **92**, 451–456.

DE GENNES, P. G. 1985 Wetting: statics and dynamics. *Rev. Mod. Phys.* **57**, 827–863.

DUSSAN V., E. B. 1979 On the spreading of liquids on solid surfaces: static and dynamic contact lines. *Ann. Rev. Fluid Mech.* **11**, 371–400.

GASKELL, P. H., SAVAGE, M. D., SUMMERS, J. L. & THOMPSON, H. M. 1995 Flow topology and transformation in a fixed-gap symmetric forward roll coating systems. In *Ninth Intl Conf. on Numerical Methods in Laminar and Turbulent Flow* (ed. P. Durbetaki & C. Taylor), pp. 984–995. Pineridge Press.

GASKELL, P. H. & SAVAGE, M. D. 1995 Meniscus roll coating. In *Liquid Film Coating* (ed. S. F. Kistler & P. M. Schweizer). Chapman and Hall – to appear.

GREENER, J. & MIDDLEMAN, S. 1975 A theory of roll coating of viscous and viscoelastic fluids. *Polymer Engng Sci.* **15**, 1–10.

GREENER, J. & MIDDLEMAN, S. 1979 Theoretical and experimental studies of the fluid dynamics of a two-roll coater. *Ind. Engng Chem. Fundam.* **18**, 35–41.

HINTERMAIER, J. C. & WHITE, R. E. 1965 The splitting of a water film between rotating rolls. *TAPPI J.* **48**(11), 617–625.

HOOD, P. 1976 Frontal solution program for unsymmetric matrices *Intl J. Numer. Meth. Engng* **10**, 379–399.

HUGHES, T. R. J. 1987 *The Finite Element Method: Linear Static and Dynamic Finite Element Analysis.* Prentice-Hall.

JOSEPH, D. D. & STURGES, L. 1978 The convergence of biorthogonal series for biharmonic and stokes flow edge problems: Part II. *SIAM J. Appl. Maths* **34**, 7–26.

KISTLER, S. F. & SCRIVEN, L. E. 1983 Coating flows. In *Computational Analysis of Polymer Processing* (ed. J. R. A. Pearson & S. M. Richardson) pp. 243–299. Appl. Sci. Publishers.

LANDAU, L. & LEVICH, B. 1942 Dragging of a liquid by a moving plate. *Acta Physicochimica URSS* **XVII** (1-2), 42.

MALONE, B. 1992 An experimental investigation of roll coating phenomena. PhD thesis, University of Leeds.

PAN, F. & ACRIVOS, A. 1967 Steady flows in rectangular cavities. *J. Fluid Mech.* **28**, 643–655.

PEARSON, J. R. A. 1985 *Mechanics of Polymer Processing*, pp. 378–380. Elsevier.

PITTS, E. & GREILLER, J. 1961 The flow of thin liquid films between rollers. *J. Fluid Mech.* **11**, 33–50.

RUSCHAK, K. J. 1982 Boundary conditions at a liquid/air interface in lubrication flows. *J. Fluid Mech.* **119**, 107–120.

RUSCHAK, K. J. 1985 Coating flows. *Ann. Rev. Fluid Mech.* **17**, 65–89.

SAVAGE, M. D. 1982 Mathematical models for coating processes. *J. Fluid Mech.* **117**, 443–455.

SAVAGE, M. D. 1984 Mathematical models for the onset of ribbing, *AIChE J.* **30**, 999–1002.

SCHNEIDER, G. B. 1962 Analysis of forces causing flow in roll coaters. *Trans. Soc. Rheol.* **6**, 209–221.

SHANKAR, P. N. 1993 The eddy structure of stokes flow in a cavity *J. Fluid Mech.* **250**, 371–383.

THOMPSON, H. M. 1992 A theoretical investigation of roll coating phenomena. PhD thesis, University of Leeds.

ZIENKIEWICZ, O. C. 1982 *The Finite Element Method*, 3rd Edn. McGraw Hill.